Tellus (1989), *41B*, 177–195

Investigating the transfer processes across the free aqueous viscous boundary layer by the controlled flux method

By B. JÄHNE[1]*, P. LIBNER[1], R. FISCHER[1], T. BILLEN[1] and E. J. PLATE[2], [1]*Institut für Umweltphysik, Universität Heidelberg Im Neuenheimer Feld 366, D-6900 Heidelberg;* [2]*Institut für Hydrologie und Wasserwirtschaft, Universität Karlsruhe, Kaiserstraße 12, D-7500 Karlsruhe, FRG*

(Manuscript received 25 January 1988; in final form 6 April 1988)

ABSTRACT

Theory and experimental results of a new method are described directly investigating the transfer processes across the aqueous viscous boundary layer. The method is based on a known and controllable flux density being applied at the interface. Then the local transfer velocity can be determined by monitoring the tracer concentration at the water surface within minutes. Moreover, the time constant for the transport across the boundary layer ("surface renewal time") can be measured directly. Comparison of the theoretical and measured frequency response of the boundary layer yields significant deviations. The technique is put into operation for heat transfer measurements. Direct comparisons with gas exchange measurements in several wind/wave facilities verify that the gas transfer velocity can be accurately extrapolated from the heat transfer measurements. A new way is opened both for detailed studies of the transfer processes in wind/wave facilities and the urgently needed direct parameterization of the transfer velocity as a function of windshear, wave parameters, and water turbulence in natural systems as rivers, lakes and the ocean. This paper includes (as a first example) measurements on the fetch dependency of the transfer process.

1. Introduction

Transfer across the air–water interface is a process linking oceans and atmosphere, the two most important reservoirs in the global cycling of chemical species. While the transfer of momentum and heat is governed by the air side, the transfer of moderately soluble and slowly reacting species, among them as important ones as CO_2, O_2, CH_4, halocarbons, and many organic compounds, is controlled by the aqueous boundary layer. Because of the small diffusion coefficient D of the gaseous species in water (and correspondingly, the high Schmidt number $Sc = \nu/D$, where ν is the kinematic viscosity) and because of the strong decrease of turbulent mixing towards the interface, the majority of the concentration change is limited to a layer of 30 to 300 μm thickness, roughly one order of magnitude thinner than the viscous sublayer (Jähne, 1985).

Despite a large number of investigations in wind/wave tunnels and in the field (for a recent review see Brutsaert and Jirka, 1984; Jähne et al., 1987a), the basic parameters controlling the transfer processes across the aqueous boundary layer at a free, wavy air–water interface gas exchange are not well established.

One of the most striking phenomena is the large enhancement of gas exchange at the onset of waves (Broecker et al., 1978; Jähne et al., 1979; McCready and Hanratty, 1984; Jähne et al., 1984, 1985 and 1987a). Only very recently, the first plausible but still speculative theoretical explanations have been undertaken (Kitaigorodskii, 1984; Coantic, 1986). Both seem not to agree with experimental results (Jähne et al., 1987a). Another important topic, lacking both theoretical understanding and detailed exper-

* Present affiliation: Scripps Inst. of Oceanography, University of California, San Diego, La Jolla, CA 92093, USA.

imental investigation, is the influence on the transfer process of the combined action of wind shear and bottom turbulence, which is a common situation in rivers (Plate and Friedrich, 1984).

In view of the very thin boundary layer for mass transfer, it is not surprising that there is a lack of knowledge about structure and the mechanisms controlling mass transfer: It is difficult to study directly such a thin layer at a moving wavy surface. Conventional techniques do not provide any direct measurement from the boundary layer itself.

In this paper, we describe a new measuring technique which yields a much more detailed insight into the transfer processes across the free aqueous viscous boundary layer than any other technique used so far: It allows a local and instantaneous measurement of the transfer velocity and an investigation of the dynamic response of the transfer across the boundary layer.

This paper contains two parts. The first part discusses theory and experimental realization of the new method in detail. In the second part, experimental results from different wind/water-tunnels are reported. Transfer velocities obtained with the new technique are carefully compared with results from other (conventional) techniques. Finally, the fetch dependency of the transfer process is discussed.

2. Basic considerations on measuring techniques

2.1. *Conventional mass balance methods*

Conventional techniques to determine flux densities of gas tracers are mainly based on mass balance of the gas tracer in the water body. The common principle of these techniques can most easily be pointed out by using the definition of the transfer velocity k. It is given as the ratio of flux density and concentration difference across the boundary layer, i.e., between the water surface and some reference depth in the water.

$$k = \frac{j}{\Delta c}. \tag{1}$$

The transfer velocity k is then inferred from measurements of the concentration variations of a tracer in air and water. The volume and time-average flux density is given by mass balance of the tracer concentration in a volume of water V_w

$$V_w \dot{c}_w = F_w j \quad \text{or} \quad j = h_w \dot{c}_w, \tag{2}$$

where F_w, and h_w are the surface area and the effective height V_w/F_w of a well-mixed water body, respectively. The analysis yields a corresponding time constant from combining eqs. (1) and (2)

$$\tau_w = \frac{h_w}{\langle k \rangle}, \tag{3}$$

being in the order of hours (wind/wave tunnels) to weeks (ocean). It is evident that the transfer velocities obtained in this way are only mean values. First, they are integrated over a large horizontal length scale corresponding to the horizontal turbulent mixing of the surface water within the given time constant τ_w. Second, they are also averaged in time over time scales in the order of τ_w. Therefore, these integration processes prevent a detailed investigation for times shorter than τ_w.

In every linear (fetch limited) wind/water tunnel, there is always the potential discrepancy that the gas exchange rate is obtained as a mean over the whole surface, whereas all parameters controlling the exchange (such as friction on the surface, water turbulence, waves) are measured locally. If only one critical parameter strongly changes with fetch, any parameterization becomes questionable.

In lakes and the ocean, a parameterization is nearly impossible since natural changes of the parameters (e.g., wind speed) are some orders of magnitude faster. This illustrates the basic point that mass balance methods are not suitable for a detailed parameterization of the exchange rates in natural systems.

In view of these severe limitations for a better understanding, two new approaches have been proposed recently. In the following two sections it is discussed what improvements are possible with these methods.

2.2. *Purposefully injected tracers*

Using natural tracers to measure air–sea gas exchange rates often involves two problems. First, the measuring procedure is complicated and time consuming. Second, the mass balance contains many other sources and sinks besides

air–sea gas exchange. These two problems may be overcome if a suitable tracer is chosen which is injected into the natural system.

Indeed, the work done by Wanninkhof et al. (1985, 1987) using sulfur hexafluoride (SF_6) is promising. This tracer can easily be measured down to ppt levels with ECD gas chromatography. So far, gas exchange results have been reported from lakes, but the low concentrations also suggest that a tracer experiment may also be successful in the ocean.

But though artificial tracer may solve the problem of closing the mass balance, the basic problem remains. The response time of the mass balance method is much too slow to yield a true and instantaneous parameterization of the gas exchange rate with the natural fluctuations and changes of the meteorology and the waves.

2.3. *Direct flux measurements*

This is a standard method in micro-meteorology, i.e., for tracers controlled by the boundary layer in air (momentum, heat and water vapor fluxes). Direct measurements of the air–sea fluxes of gas tracers are very attractive for many reasons. In the context of this paper, here the high time resolution of several minutes is the most essential point.

Unfortunately, large experimental difficulties arise when these techniques are applied to gas tracers controlled by the aqueous boundary layer, since in this case the concentration difference in the air is only a small fraction of the concentration difference between bulk water and bulk air. Consequently, the resulting relative tracer gradients are very low (at most a few percent (Roether, 1983)).

Therefore it is not surprising that no reliable data have been obtained so far. Direct air–side flux measurements of air–sea CO_2 fluxes by eddy correlation technique as reported by Wesely et al. (1982) and Smith and Jones (1985) give much too high transfer velocities, completely inconsistent with all other field and laboratory investigations of air–sea gas exchange (Broecker et al., 1986). Other tracers as radon and methyliodide (CH_3I) have also been proposed for direct flux measurements (Roether, 1983), but no measurements have been reported to this day. Substantial work is necessary to get direct air–side flux measurements working. Even if a sufficient measuring sensitivity can be achieved, it has to be proven that there are no systematic errors by effects like lateral inhomogeneity and unsteady micro meteorology.

2.4. *Controlled flux method*

In this paper, a completely different approach is presented. It directly investigates the boundary layer with remote instruments. It is a universal technique, being suitable both for laboratory and field measurements, and it allows much more detailed investigations, since the transfer velocity is measured locally and with a fast response time in the order of minutes.

The new technique is based on a simple idea, explained most easily by using the definition of the transfer velocity, eq. (1). Conventional techniques (as discussed above) start from given or manipulated concentration differences and determine the transfer velocity from the measured flux density. The new method is the inversion of this procedure. A controllable tracer flux is forced onto the water surface and the transfer velocity is determined from eq. (1) by means of the measured concentration difference at the water surface and in the bulk.

Though this idea is so simple, it has far-reaching consequences. Consider a simple thought experiment. Let the system be in equilibrium with respect to the tracer concentrations in air and water. Then the tracer concentration at the water surface is equal to the bulk water-concentration. Now switch on a constant tracer flux density at the interface. Immediately, the tracer's surface-concentration increases; eventually, it reaches an equilibrium value at which the incoming flux density is balanced by the flux density across the aqueous boundary layer. Since almost all resistance to the transfer process is concentrated near the surface, only the boundary layer itself is involved in concentration changes. Therefore, this process is controlled by the length and time scales of this layer.

The characteristic vertical length scale is the thickness of the mass boundary layer. Consequently, the corresponding time constant indicates the time necessary for the tracer to pass the viscous boundary layer. Independent of any assumptions about the transport mechanism, these scales can be defined as follows. The boundary layer thickness z_* ("film thickness") is

given by

$$z_* = \frac{D}{\langle k \rangle}. \tag{4}$$

This is the fictitious thickness of a rate controlling layer in which transfer occurs by molecular transport only. Geometrically, z_* is given as the interception of the tangent to the concentration profile, at the air–water interface, with the bulk (or some other reference) concentration level (Fig. 1). With the help of z_* the time constant t_* can now be defined as

$$t_* = \frac{z_*}{\langle k \rangle} = \frac{D}{\langle k \rangle^2}. \tag{5}$$

In comparison to the mass balance methods (cf. eq. (3)), the time scale of the new technique is reduced by the ratio of the effective height h_w of the water body to the thickness of the aqueous mass boundary layer z_*. The time constant is of the order of only 0.1 to 10 s. This fast response of the surface layer ensures that it is sufficient to measure the surface concentration in order to obtain the transfer velocity, since the bulk concentration remains constant in such short time scales. Indeed, the bulk concentration can be determined directly at the surface, if the flux density is switched off. Consequently, the concentration difference can be measured with a single probe.

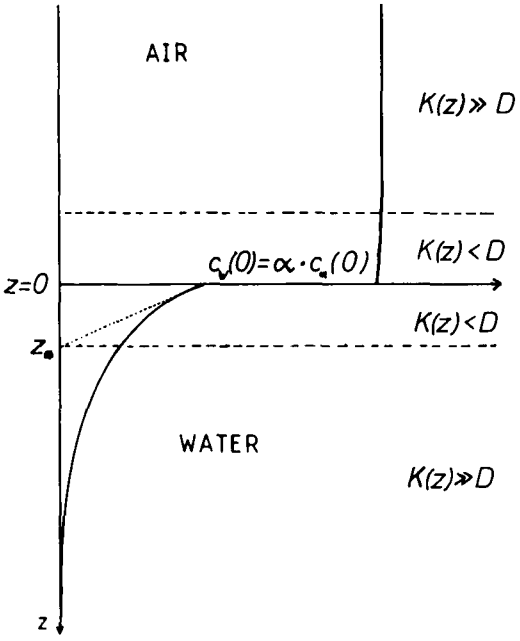

Fig. 1. Schematic diagram of the aqueous boundary layer of mass transfer, showing the mean gas concentration profile and explaining the definition of the boundary layer thickness z_*. K is the eddy diffusivity; D is the molecular diffusivity, z is defined positive downwards.

3. Theory of the controlled flux method

3.1. Direct measurement of "surface renewal rate"

Conventional measuring techniques yield no direct information on the time constant for mass exchange. It can only be calculated indirectly by means of eq. (5). At this point, it should be emphasized that the determination of the mean transfer velocity $\langle k \rangle$, the boundary layer thickness z_*, or the time constant t_* are equivalent modes of study. If one quantity is measured, the two others can be obtained by means of eqs. (4) and (5). The three quantities reflect the flux, the length, and the time scales of the process, and are coupled by the molecular diffusion coefficient. It will now be shown how the time constant can be measured directly.

The time constant can be determined by examining how the boundary layer responds to a periodically varying flux density on average. As long as the frequency ω ($\omega = 2\pi f$) is low compared with t_* (i.e., $\omega t_* \ll 1$), the mean amplitude of the surface concentration remains constant at the (equilibrium) value for zero frequency. But if the frequency is increased, the amplitude starts lagging behind the flux density and decreasing. These effects directly depend on the time constant t_*. Consequently, an analysis of the frequency response of the boundary layer on a periodically varying flux density allows a direct determination of t_*.

3.2. Frequency response and turbulent structure

Such an analysis provides additional insight into the structure of the boundary layer: The larger the frequency, the shallower the tracer will penetrate. Therefore, the structure of turbulence with depth can be probed. Although only measur-

ing the surface concentration, we shall nevertheless obtain more detailed information on the increase of turbulence with distance from the surface. This approach yields such information, because it is an active probing of the mass boundary layer with a variable input function.

The method applies typical concepts of linear signal theory to the mass-transfer problem. The features of the "black box" mass boundary layer are investigated by measuring the input/output relation of the system, where the input into the system is the applied flux density and the output is the surface temperature. The general behavior of the boundary layer is similar to a low-pass filter. We will now discuss how the structure of the turbulence in the boundary layer affects the frequency response. Two different approaches are chosen, in order to get an idea of the sensitivity. Both models are restricted to horizontal homogeneity and to non-reacting species.

First, a generalized surface renewal model (SR-model) is used to characterize the turbulent structure. In this model, large eddies play the dominant role, statistically sweeping the whole of the surface layer or part of it into the bulk liquid. The surface renewal rate λ is assumed to depend on the distance z from the surface with a power law

$$\lambda = \gamma_p z^p \quad \text{with} \quad p \geqslant 0. \tag{6}$$

For $p = 0$ we have the classical surface renewal model where the renewal rate does not depend on the distance from the surface and $\gamma_0 = t_*^{-1}$. For $p > 0$, the very surface is not renewed. This is necessarily the case, even for a free water surface, as soon as it is contaminated by a high-surface-pressure film hindering flow convergence or divergence at the surface (Jähne, 1985; Jähne et al., 1987a).

A second model is a multi-stage small-eddy model (K-model). In this model, the turbulent transport term is expressed by a local turbulent diffusion coefficient changing with depth according to a power law

$$K = \alpha_m z^m \quad \text{with} \quad m \geqslant 2. \tag{7}$$

These two models represent two extremes; physical reality is likely to be somewhere in between. For large m and p, both models coincide with the film model with its stagnant diffusive layer of constant thickness and without any turbulence at the surface (Liss and Slater, 1974). The exponents m and p are directly related to the dependence of the transfer process on molecular diffusion coefficient and Schmidt number. The following proportionalities are obtained for high Schmidt numbers (Jähne, 1985)

$$\begin{aligned}
&\text{(K)} \\
&z_* \propto D^{1/m} \qquad t_* \propto D^{-(m-2)/m} \quad \langle k \rangle \propto D^{(m-1)/m} \\
&\text{(SR)} \\
&z_* \propto D^{1/(p+2)} \quad t_* \propto D^{-p/(p+2)} \quad \langle k \rangle \propto D^{(p+1)/(p+2)}
\end{aligned} \tag{8}$$

The same power laws are obtained for $m = p + 2$.

Analytical solutions of the amplitude damping and phase shift can be derived only for the film model ($p \to \infty$, $m \to \infty$) and the classical surface-renewal model ($p = 0$). For all other models, numerical calculations were made (see appendix A). The results for amplitude damping and for the phase shift between the flux density and the surface concentration are shown in Fig. 2 as a function of the dimensionless frequency $\omega_+ = \omega t_*$.

For high frequencies ($\omega_+ > 10$), all models agree in a constant phase shift of $\pi/4$ and an amplitude damping proportional to $\omega_+^{-1/2}$. The cause is that, at high frequencies, the penetration depth is much lower than the boundary layer thickness and is restricted to the region dominated by molecular diffusion. This is an important conclusion, being independent of any model considerations (ignoring chemical reactions).

The result allows a direct determination of t_* from the amplitude damping at high frequencies. In the dimensionless graph, the $\omega_+^{-1/2}$-damping line crosses unity at $t_* = 1$. Consequently, in a graph showing the measured amplitude as a function of the ω, the $\omega^{-1/2}$-line meets the horizontal line of the undamped amplitude at t_*^{-1}.

It is important to note that it is not necessary to know the flux density in order to determine t_*. On the contrary, it is possible to check or calibrate the flux density in this way, since for high frequencies, the concentration amplitude is generally given by

$$|\tilde{c}_s| = \frac{|\tilde{j}|}{(D\omega)^{1/2}}. \tag{9}$$

The only unknown in this equation is the flux density.

At low frequencies (i.e., $\omega_+ < 1$), the amplitude remains constant up to $\omega_+ = 0.3$ and the phase

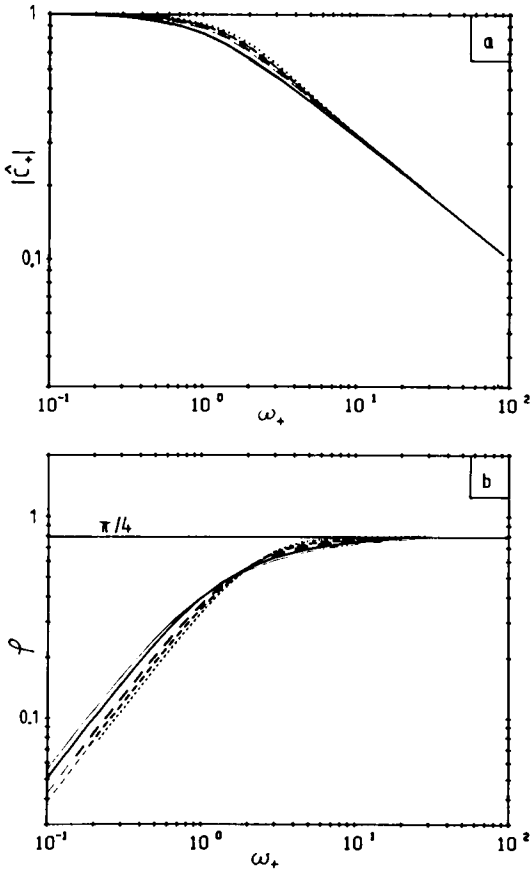

Fig. 2. Amplitude attenuation (a) and phase shift between the flux density at the water surface and surface concentration periodicity (b), with the boundary condition of a forced sinusoidal flux density at the surface. The results of model calculations are shown as a function of the dimensionless frequency ω_+. Line key: thick lines: surface renewal models; thin lines: diffusion models; line type indicates the Schmidt number exponent n: solid line: 1/2; long-dashed line 3/5; short dashed: 2/3; dotted: 3/4.

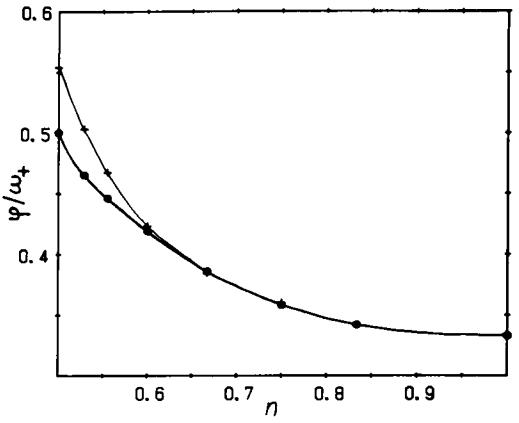

Fig. 3. Phase shift $\varphi_+ = \varphi/\omega_+$ for low ω_+ as a function of the Schmidt number exponent for surface renewal models (circles and thick line) and diffusion models (pluses and thin line).

shift φ increases linearly with ω_+ up to $\omega_+ = 0.5$

$$\varphi = \kappa\omega_+, \tag{10}$$

where κ is a model-dependent constant between 0.33 and 0.55. From Fig. 2, it is obvious that the phase shift for low frequencies most clearly distinguishes the different models. But it can also be seen from Fig. 2b that the structure of the turbulence can hardly be detected by the phase shift: The SR and D-models more-or-less coincide for the same Schmidt number dependence of the transfer rate. Fig. 3 shows more details of the phase-shift at low frequencies as a function of the Schmidt number exponent n for both types of models. There are only small differences for n near 1/2. Since the exponent n for free surfaces can vary only from 1/2 to 2/3 (Jähne, 1985), it can be determined by the phase shift changing sensitively in this range. An accuracy of about 5% in the phase shift is necessary to determine n with an uncertainty of about 0.03.

The analysis of the frequency response of the mass boundary layer with a forced periodically changing flux density therefore yields similar information as measurement with two tracers differing in the diffusion coefficient. Only the average effect of the turbulence increase with depth can be determined, but obviously no more details about the structure of the turbulence can be deduced. Nevertheless, the frequency analysis with the method of controlled flux offers the advantage of measuring the Schmidt number dependence of the transfer with a single tracer.

4. Experimental realization

4.1. Principle

To apply the controlled flux method, a controlled flux density must be applied at the air–water interface and the surface concentration

must be measured. Both requirements are most easily met if heat is used as a tracer. First, the forced periodic flux can be realized by a chopped infrared radiator. Second, the surface temperature can be measured by an IR-radiometer.

Fig. 4a illustrates the thermal boundary layer under these conditions. Since the Schmidt number is about 100 times lower for heat than for gases dissolved in water, the thermal boundary layer is not thinner than 100 μm even for high wind speeds of about 15 m/s. Yet the thermal boundary layer is still about three times thinner than the viscous boundary layer (Jähne, 1985). Extrapolation from heat transfer velocities to gas transfer rates will be discussed in Section 5.

Infrared radiation is strongly absorbed by water: 1000 K radiation (2–6 μm) penetrates only about 20 μm into the water. Since the main resistance for heat transfer lies in the air-phase boundary layer, nearly all (about 97%, (Jähne, 1982), Fig. 4) of the heat flux density flows across the aqueous boundary layer into the bulk water. Fig. 4 also compares typical latent and sensible heat flux densities with the artificially applied radiation across the aqueous boundary layer. The applied radiation is comparable to or even lower than the typical heat fluxes due to sensible heat transfer and evaporation. Nevertheless, it is possible to measure the heat-transfer velocity accurately. Because of the periodic variation of the artificial IR-radiation, the spectrum of the surface temperature signal consists of high narrow peaks. Therefore, systematic (constant and statistically fluctuating) deviations of the surface temperature by sensible, latent, and radiative heat transfer are strongly suppressed. This fact is very advantageous, especially for field measurements. In contrast to the conventional measurement of the heat transfer velocity in water (Hasse, 1971; Paulson and Simpson, 1981), it is not necessary to measure the sensible and latent heat fluxes. Additional errors because of the uncertainty of the difference between surface and bulk temperatures are avoided. Moreover, the low heat flux necessary for the transfer measurements ensures that the transfer processes are not influenced by buoyancy effects.

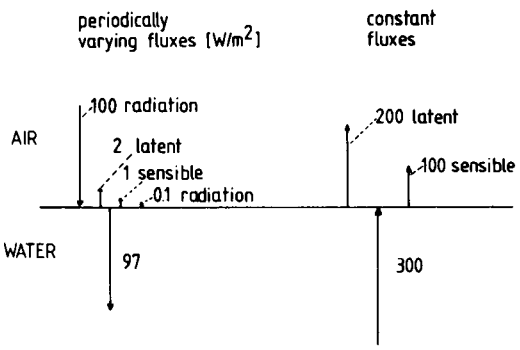

Fig. 4. Comparison of the different periodic varying heat flux densities due to the application of the controlled flux method with the constant heat flux densities due to evaporation and sensible heat exchange.

The radiometer which is sensitive in the 8–14 μm wavelength range measures the temperature of about the top 10 μm of the boundary layer. Consequently, both requirements are well approximated: a controllable heat source is put onto the water surface efficiently forcing a flux across the aqueous boundary layer, and the concentration is really measured at the surface.

4.2. Corrections due to non-zero penetration

The corrections due to the non-zero penetration of the IR-radiation can be calculated straightforwardly. The temperature profile is less steep only in the vicinity of the penetration depth of the IR-radiation, i.e., in a region only being influenced by molecular diffusion (Fig. 5). Therefore, the decrease of the surface temperature is independent of the structure of the turbulence and simply proportional to the ratio of the penetration depth of the radiation, z_p, and the boundary layer thickness z_*. The calculations outlined in appendix A.6 yield for small chopper frequencies ($\omega_+ < 0.3$)

$$\frac{T_s}{T_{s0}} = 1 - \frac{z_p}{z_*}, \tag{11}$$

where the index 0 marks the surface temperature for zero penetration of the IR-radiation. A similar correction has to be applied for the phase shift

$$\varphi = \kappa\omega_+\left(1 + \frac{z_p}{z_*}\right). \tag{12}$$

Because of the resulting flat temperature profile at the interface (Fig. 5), no additional corrections are necessary due to the even lower penetration depth of the temperature measurement.

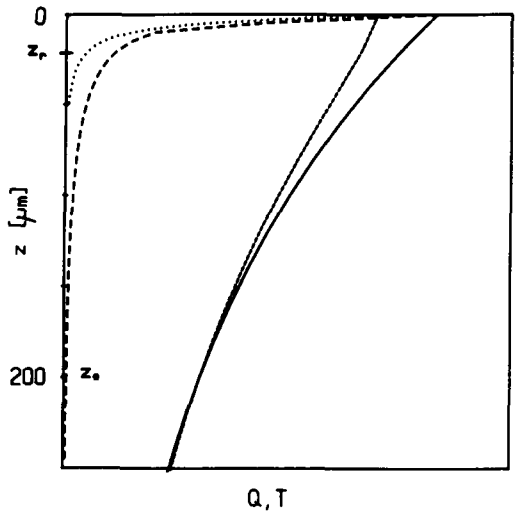

Fig. 5. Illustration of the thermal boundary layer for application of the controlled flux method. Several profiles are shown: dashed line: distribution of the heat source (i.e., absorbed IR-radiation); dotted line: surface temperature measurement; solid line: ideal temperature profile; dashed-dotted line: real profile calculated using the heat source distribution shown.

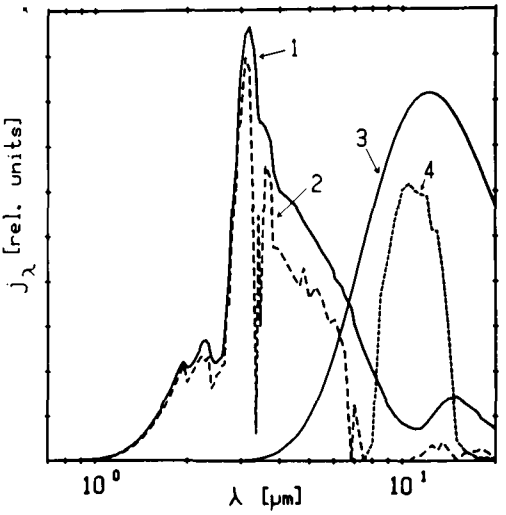

Fig. 6. Wavelength separation between the IR-radiation irradiated onto the water surface and the radiation emitted by a 300 K water surface used to measure its temperature using a radiometer: 1000 K radiation reflected by the water surface (1); same but filtered by a 100 and 25 μm Hostaflon foil (2); 300 K radiation (3); part of the 300 K radiation seen by the radiometer through the 8 to 14 μm band pass filter (4).

4.3. Horizontal homogeneity

Another problem has to be considered for an appropriate application of the controlled flux method. In the analysis, it was assumed that the IR-radiation is horizontally homogeneous. In reality, this cannot be the case. The footprint of the IR-radiation has a limited size. Therefore, it must be assured that a water surface element stays long enough in the radiated area, say several time constants, t_*. This allows a simple estimate of the required size of the irradiated spot. A water surface element travels with a surface drift velocity of the order of 10 cm/s (about 2 to 3% of the wind speed). Since the time scale t_* is about 1 s, the horizontal length scale x_* for a water surface element to come into equilibrium with the radiation, is about 10 cm. The diameter of the footprint of the IR-radiator on the water surface must therefore be some 10 cm for correct measurements.

4.4. Suppression of irradiation for surface temperature measurements

The radiometer must not measure any backscatter from the radiator, otherwise the surface temperature measurements would be falsified. The requirements for this separation are quite high, since the radiometer should detect very small temperature differences. If a maximal temperature error of 10^{-3} K is allowed, the additional artificial IR-radiation of the radiator seen by the radiometer must be lower than 13 ppm of the radiation from the water surface (420 W/m^2 at 20°C) i.e., $5.6 \cdot 10^{-3}$ W/m^2; however, as much as 100 W/m^2 are irradiated by the radiator. Though only 2% of them are reflected, the interference signal of 2 W/m^2 is about three orders of magnitude higher than the required measuring accuracy.

Two methods are used simultaneously to suppress the influence of backscattered IR-radiation from being seen by the radiometer: wave length separation and geometrical separation (Libner, 1987).

While the radiometer is equipped with a bandpass filter transmitting only wavelengths between 8 and 14 μm, the long wave lengths emitted by the 1000 K radiator are cut off using a set of ventilated Hostaflon foils. Fig. 6 shows that the filter-set considerably blocks the long wavelengths, but not entirely.

In addition, geometrical blocking is used. Radiator and radiometer are arranged in such a way that no radiation can be backscattered into the radiometer in the case of a smooth water surface. But even with a wavy surface, where the incoming IR-radiation is sometimes reflected into the radiometer, the probability for reflexes is low.

4.5. Experimental set-up

Experiments were conducted in the wind/wave facility of the University of Karlsruhe and in the circular wind/wave facilities of the Institut für Umweltphysik in Heidelberg. Fig. 7 illustrates the experimental set-up used in Karlsruhe. (A similar arrangement was used in Heidelberg.) A 3000 W IR-radiator is installed 75 cm above the water surface. It can be chopped with frequencies up to 2 Hz using hydraulically moving screens. The footprint of the radiation has a half-value diameter of 54 cm. The radiometers (KT-4, Heimann, Wiesbaden, and in some experiments a Barnes PRT-5) were looking at the center of the spot at an angle of about 23° to the normal to the water surface, so that they do not receive reflected radiation from the radiator as long as the slope of the water surface is lower than 0.16. The diameters of the measuring spot at the water surface are 1.7 and 5 cm for the KT4 and PRT5, respectively.

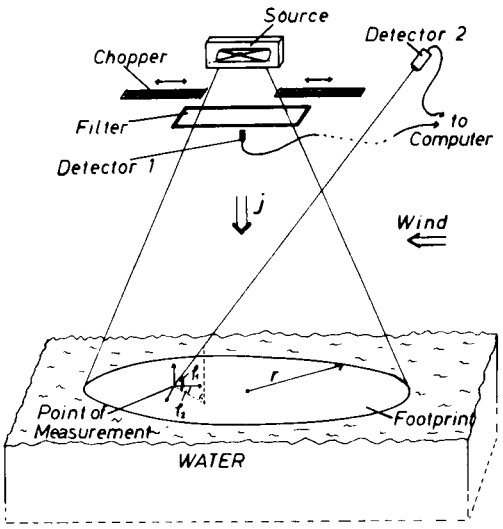

Fig. 7. Outline of the experimental arrangement used in the wind/wave facility of the Institut für Hydrologie und Wasserwirtschaft, University of Karlsruhe, for the local heat transfer measurements.

5. Results

This section contains four parts. First, the surface temperature signal itself is discussed with the intention of verifying that the controlled flux method operates as theoretically expected. Second, the frequency response of the boundary layer (amplitude damping and phase lag of the surface temperature as a function of the chopper frequency) is compared to the theoretical predictions. Third, the transfer velocities obtained are reported. Special emphasis is put on the question of how the transfer velocities for gases can be extrapolated from the heat transfer measurements. Finally, we make use of the fact that the transfer velocities are measured locally, and present data on the fetch dependency of the transfer process.

5.1. The surface temperature signal

Fig. 8 shows the response of the surface temperature on infrared radiation switched on and off with a period of 1 min at two different wind speeds (2.5 and 5.7 m/s). While the signal in a single-sample record (left side) just escapes the noise level of the radiometers, it is clearly visible in the in-phase average signal (right side) over 16 records.

The change in the surface temperature is about 0.5 K at the low wind speed, but only 0.2 K at the higher wind speed. Since the flux density is the same at both conditions, the transfer velocity is inversely proportional to the temperature change (eq. (1)). In this way, we can immediately conclude that the relative transfer velocity, is 2.5 times higher at 5.7 m/s than at 2.5 m/s wind. A calibration of the incoming radiation gives the absolute values of the transfer velocities.

The surface temperature signal in Fig. 8 directly shows the time response of the boundary layer for a changing flux density. The time response is much slower at the low wind speed than at the higher wind speed. This is also theoretically expected, since the time constant t_* is inversely proportional to the square of the transfer velocity (eq. (5)) which is itself roughly proportional to wind speed.

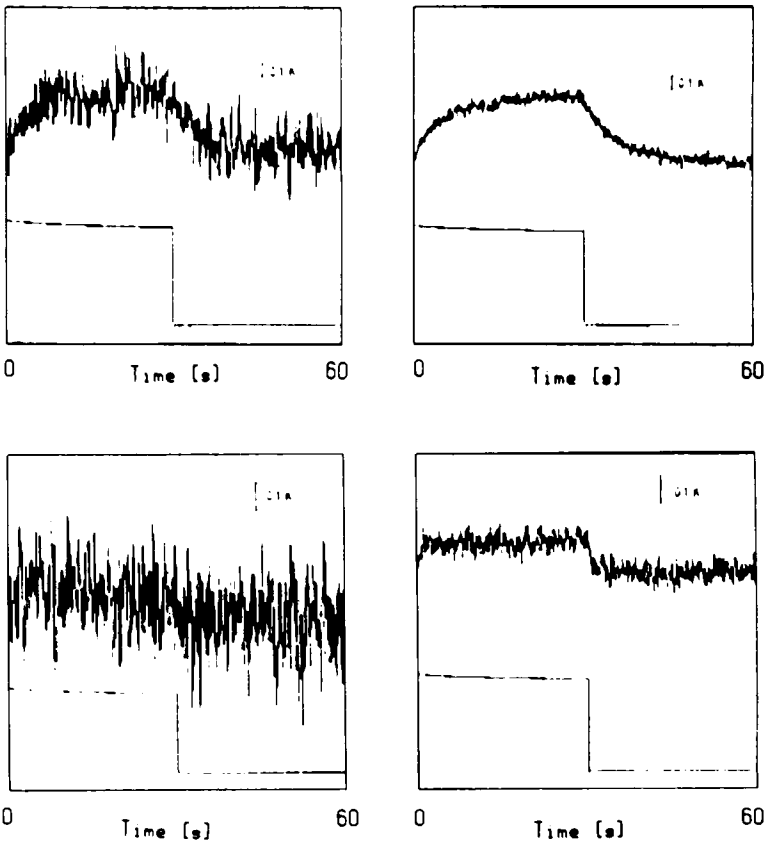

Fig. 8. Original (left side) and averaged time series of the surface temperature (right side) at low (2.5 m/s, upper figures) and medium (5.7 m/s, lower figures) wind speed. The corresponding heat flux signal at the water surface is shown as a dashed line.

From this settling to the equilibrium surface temperature, we can directly estimate t_* to be about 8 s. This is a direct determination of the time scale of the exchange process, from which we may independently calculate a transfer velocity. This illustrates that the constant flux method offers two independent ways to determine the transfer rate.

5.2. *Frequency response of the surface temperature*

Fig. 9 shows the power spectra of the temperature signal for similar conditions as in the previous section. At the higher wind speed of 7.8 m/s, the peaks in the spectra nicely follow a f^{-2} line as expected for an undamped rectangular signal. At 3.5 m/s, the decrease of the peaks with frequency as $\sim f^{-2.5}$, as expected if the rectangular signal is damped by the transfer process by a factor $f^{-0.5}$ in the limit of high frequencies (cf. eq. (9)).

A more detailed study of the frequency response was carried out by using chopper periods between 2 s to 1 min. Fig. 10 shows the amplitude of the surface temperature increases as a function of the chopper frequency in a double logarithmic plot. At higher wind speed, the amplitude signal is low, but remains constant. Towards lower wind speed, the amplitude starts decreasing more and more earlier. As predicted theoretically (eq. (9)), the amplitude signals finally all coincide at high frequencies, where the amplitude goes as $\omega^{-1/2}$. This line is used to calibrate the flux density according to eq. (9).

Now the most interesting question is, how the measured amplitude damping and phase lag of the surface temperature signal compare with the

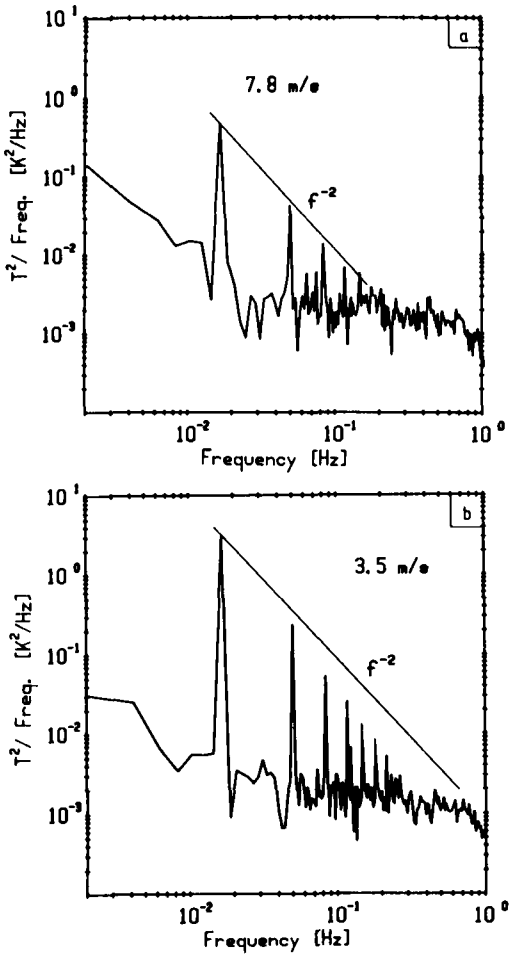

Fig. 9. Power spectra of the surface temperature response on a switched heat flux in a double logarithmic plot for two wind speeds as indicated.

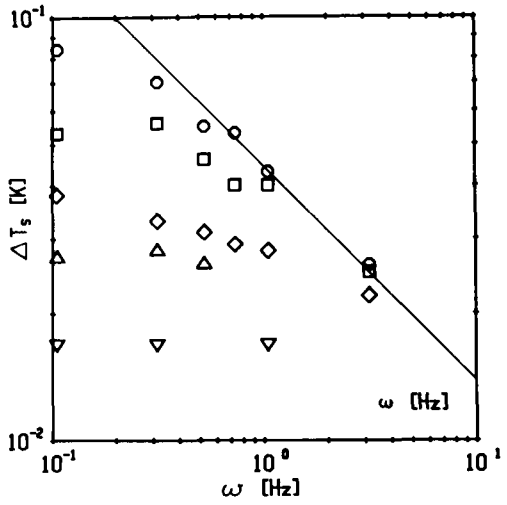

Fig. 10. Amplitude of the water surface temperature signal as a function of the chopper frequency; symbol key for wind speed (m/s): crosses 3.5, squares 5.2, diamonds 7.8, triangles 10.7, tilted triangles 13 m/s.

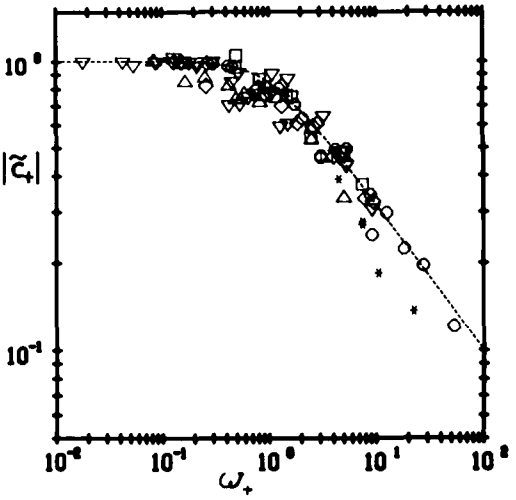

Fig. 11. Measured amplitude damping as a function of the dimensionless frequency ωt_* in a double logarithmic plot. Symbol key for wind speed classes (m/s): stars <3.2, circles <4.2, squares <5.6, diamonds <6.7, triangles <7.7. tilted triangles >7.7. The solid line represents the theoretical prediction by the surface renewal model with $n = 1/2$.

theoretical predictions as discussed in Section 3. In order to get a good data basis, we first calculated t_* for all conditions from the measured surface temperature increase at low frequencies. It is then possible to present the data in dimensionless plots where the amplitude damping (Fig. 11) and the phase lag (Fig. 12) are shown as a function of ω_+.

Roughly, both the amplitude damping and the phase lag agree with the theoretical predictions. But there are some remarkable differences. First, the amplitude damping is 10–20% lower in the transition region around $\omega_+ \approx 1$. This means that the amplitude damping starts earlier than expected in all models.

Even more significant deviations from the theoretical predictions are found for the phase

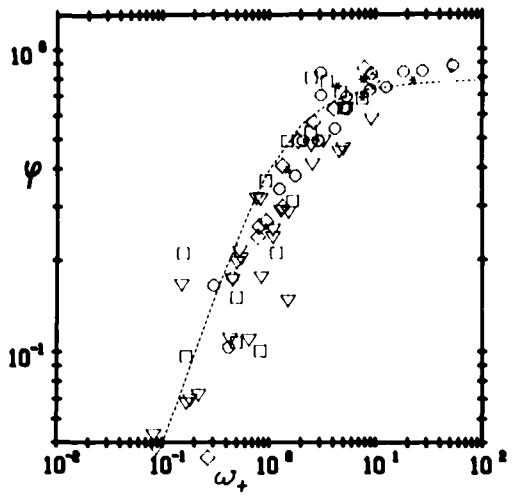

Fig. 12. Measured phase shift as a function of the dimensionless frequency ωt_* in a double logarithmic plot. Key to symbols, see Fig. 11. The solid line represents the theoretical prediction by the surface renewal model with $n = 1/2$.

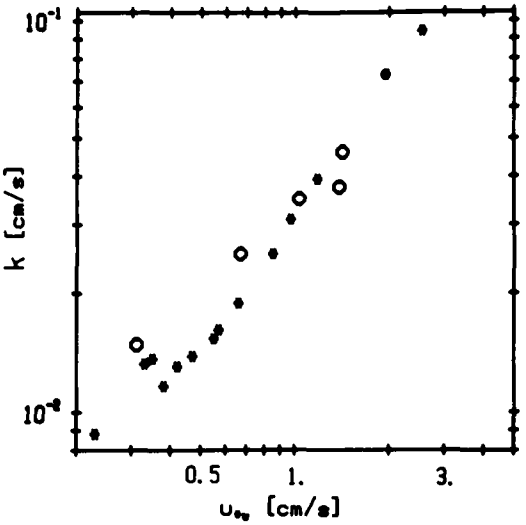

Fig. 13. Comparison of the transfer velocities of heat across the aqueous boundary layer measured by the evaporation method (stars) and the controlled flux method (circles). Measurements are from the circular wind/wave facility, Heidelberg.

shift. While at high ω_+ it reaches the predicted value of $\pi/4$, it is considerably lower at small ω_+. The model calculations result in a linear increase of the phase shift φ with ω_+, i.e., $\varphi = \kappa\omega_+$, where κ ranges between 0.33 for the film model to 0.5 for the surface renewal model. The experimental results indicate a mean κ of about 0.3, which is even lower than the lower limit of the calculations. This fact is even more surprising, since it is known that the Schmidt number exponent is 0.5 for the results shown here, corresponding to κ around 0.5.

Consequently, these results strongly suggest that the simple models do not describe the transfer process adequately. In principle, this is not surprising, since the complex stochastic process of transfer across the boundary layer has been modeled by a one-dimensional linear process.

The data can therefore be used as a test for much more detailed modeling of the structure of turbulence in the boundary layer.

5.3. *Transfer velocities*

In this section, the transfer velocities are discussed. In Fig. 13, heat transfer velocities obtained by the controlled flux method and the evaporation method in the large circular wind-wave facility are compared to each other. With the latter method, the transfer velocity is determined by measuring the latent heat flux due to evaporation and the corresponding surface temperature decrease (Jähne, 1985). The results agree very well with each other (mean deviation less than a few percent), verifying that the controlled flux method yields correct heat transfer rates.

Our basic goal is to determine the air-sea gas transfer rates by the constant flux methods. The measured transfer velocities for heat therefore have to be extrapolated to the different gases. Heat is just a scalar tracer as are gases. Only the diffusion coefficient for heat is about two orders of magnitude higher than for gases, but the dependence of the transfer velocity on the diffusion coefficient has been investigated in detail using different gases and heat as tracers in simultaneous measurements (Jähne et al., 1987a). The dependence can be expressed by the simple formula

$$\frac{k_1}{k_2} = \left(\frac{D_1}{D_2}\right)^n = \left(\frac{\mathrm{Sc}_1}{\mathrm{Sc}_2}\right)^{-n}, \tag{13}$$

where the (dimensionless) Schmidt number Sc is defined as the ratio of kinematic viscosity ν to the diffusion coefficient D, $\mathrm{Sc} = \nu/D$. The exponent n ranges between 1/2 and 2/3 depending on the

friction velocity and the mean square slope of the waves (Jähne et al., 1987a). The diffusion coefficients of different gas tracers are known accurately enough, so as not to introduce additional errors into the extrapolation (Jähne et al., 1987b).

Fig. 14 shows a comparison of extrapolated and measured oxygen transfer coefficients from the Karlsruhe wind/wave facility. The agreement is very convincing. Despite the large correction factor of nearly one order of magnitude, the maximum deviation is only about 20%; the mean deviation is less than 5%. There is a small, but significant trend, that the extrapolated values are higher than the directly measured one at low wind speeds. Such small deviations are not surprising, since the controlled flux method yields local transfer coefficients at a fetch of 8 m, whereas the directly measured oxygen transfer velocities are mean values integrated all over the water surface. In order to be sure about these differences, we also investigated the fetch dependence.

5.4. *Fetch dependence of transfer velocities*

The fetch dependence was studied in the linear Karlsruhe facility by leaving the instrument at the same fetch of 8 m, but covering a varying section of the water surface from the entrance with a polyethylene foil. In this way, the effective fetch was varied between 2 and 8 m. Fig. 15a shows the measured relative transfer velocities at four different wind speeds as a function of the fetch. Whereas at the highest wind speed, no significant change is observed, the reduction of the transfer velocity towards lower fetch becomes more and more pronounced at lower wind speeds.

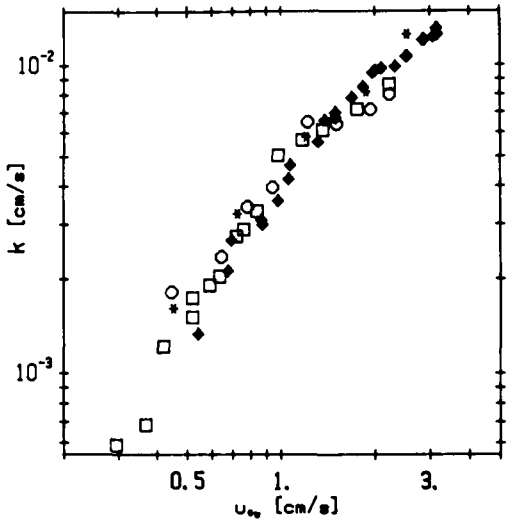

Fig. 14. Comparison of directly measured oxygen transfer velocities (solid diamonds, Wacker, personal communication) and extrapolated values from heat transfer velocities (all other symbols) across the aqueous boundary layer as obtained with the controlled flux method at 8 m fetch.

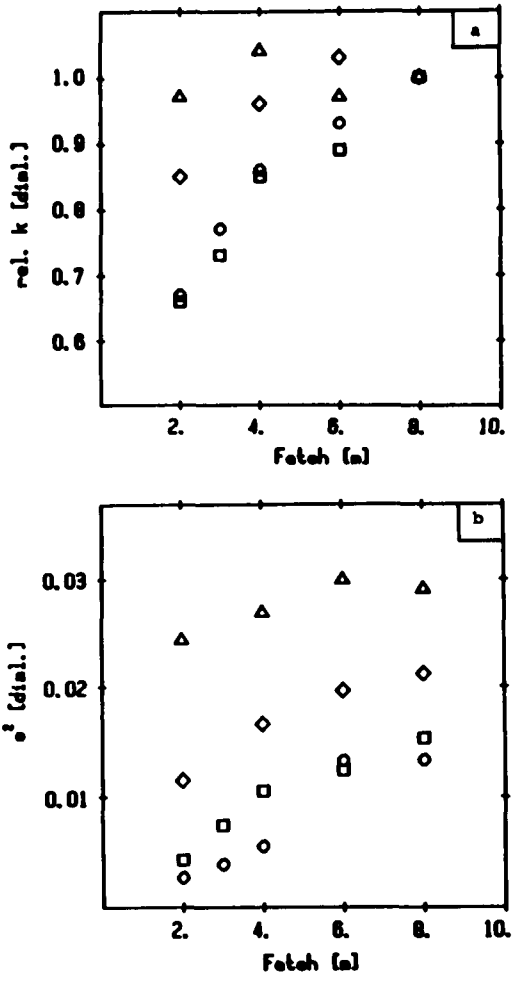

Fig. 15. Fetch dependence of the transfer process across the aqueous boundary layer: Heat transfer velocity relative to the value at 8 m fetch as a function of fetch (a). Mean squares slope of the waves relative to the value at 8 m fetch as a function of the fetch (b). Symbol key to wind speeds: see Fig. 11.

But still the effect is quite low. The maximum reduction found is about 34%.

The measured fetch dependence explains the small deviations between the directly measured and extrapolated oxygen transfer coefficients. From the measured fetch dependence at low wind speeds, we can conclude that the transfer velocity integrated over the whole water surface is about 20% lower than the local value at 8 m fetch. This is just about the factor the extrapolated local oxygen transfer coefficients at 8 m fetch are higher than the measured mean oxygen transfer velocity.

Now we turn to the question of the reason for the fetch dependence found. From previous investigations, it is known that the transfer process is very sensitive in the wave field and that the mean square slope of the waves is the best parameter to describe this influence (Jähne et al., 1987a). Fig. 15b therefore shows the relative change of the mean square slope as a function of the fetch. The mean square slope runs remarkably parallel to the transfer velocity. Only the magnitude of the change is about a factor of two larger for the mean square slope than for the transfer velocity.

We can draw two conclusions from this fact.

First, the fetch dependence is associated with the development of the wave field, so it is restricted to low fetch and low wind speed conditions. As soon as there is no change in the mean square slope, the transfer velocity also maintains a constant value.

Second, in a previous paper (Jähne et al., 1987a), we concluded that (in a first approximation) the transfer velocity is proportional to the mean square slope of the waves. The measured fetch dependence now still shows that the mean square slope is a critical parameter but that with a developing wave field at low fetches and wind speed, there is no direct proportionality. The experiments suggest that in this transition region, the relations are much more complicated and need further experimental investigation.

6. Conclusions

The experimental data obtained thus far are very encouraging. The controlled flux method clearly offers two major advantages as compared to any other experimental method.

First, it allows a very detailed investigation of the transfer processes across the aqueous viscous boundary layer. For the first time, the time response of the transfer process can be studied. Amplitude damping and phase lag roughly show the expected values as derived from standard assumptions about the turbulent structure in the boundary layer, as in surface renewal or diffusion models. But the significant deviations suggest that there are effects not understood so far and that the new technique can provide sensitive test data for a more detailed modeling of boundary layer turbulence, which is urgently needed.

Second, the new technique allows a determination of the heat transfer velocity locally and with a fast time response. Of course, it would be much better if the gas transfer velocity could be measured directly by a similar technique as the heat transfer velocity, but in this paper, we demonstrate that we can safely extrapolate gas transfer velocities from the measured heat transfer velocities. The local and instantaneous measurement of the transfer velocity opens a new way for detailed studies on the parameters influencing the transfer process. As a first example, we studied the fetch dependence in a wind/wave facility. The biggest advance can be expected for field studies. A local and instantaneous measurement of the transfer velocity allows us (for the first time) to directly investigate the dependence of the transfer processes on rapidly changing parameters such as wind speed (friction velocity) and the wave field.

We want to make use of the new technique to focus on the unsolved problem of the transfer processes under the combined action of wind and bottom-induced turbulence both in the wind/wave facility of the Institut für Hydrologie und Wasserwirtschaft, Karlsruhe, and on the Neckar river in cooperation with the Landesanstalt für Umweltschutz, Karlsruhe (Libner et al., 1987).

7. Acknowledgements

The authors gratefully acknowledge financial support from the Deutsche Forschungsgemeinschaft (German Science Foundation) for these experiments, grant Pl 60/41 "Oberflächenerneuerung". They would also like to thank the Heimann GmbH, Wiesbaden (especially Mr. Müller) for their kindness in lending us a KT4

IR-radiometer in the first phase of the project and for their readiness to cooperate with us in developing a special version of the IR-radiometer for our measurements. Likewise, the possibility to use PRT5 radiometers from the DVFLR, Oberpfaffenhofen (Dr. Misoga and Mr. Obermaier), and from the Alfred Wegener Institut für Polarforschung, Bremerhafen (Dr. Tueg), is gratefully acknowledged.

8. Appendix A. Boundary layer models

This appendix outlines the theoretical calculations for the response of the mass transport across the boundary layer on a given flux density at the surface. It is assumed that the mass transport in the boundary layer can be described by an addition of molecular and turbulent processes. The turbulent transport term is either characterized by a turbulent diffusion coefficient (K-model) or by statistical renewal of the surface layer by large eddies (SR-model).

A.1. Equations

For a nonreactive species and negligible horizontal variations, the non-steady transport equations for the mean concentration are given in the two models by

$$\begin{aligned} &\text{(K)} \quad \frac{\partial C}{\partial t} = \frac{\partial}{\partial z}\left[(D + K(z))\frac{\partial C}{\partial z}\right] \\ &\text{(SR)} \quad \frac{\partial C}{\partial t} = D\frac{\partial^2 C}{\partial z^2} - \lambda(z)\,C. \end{aligned} \tag{14}$$

The z-coordinate is defined as zero at the interface, with positive being downwards. These equations can be made dimensionless with the scale parameters for the transfer across the boundary layer: z_*, t_*, and the concentration difference Δc. Then the dimensionless quantities $C_+ = C/\Delta C$, $t_+ = t/t_*$, and $z_+ = z/z_*$ are obtained. In addition, the formulations for the turbulent diffusivity according to eq. (7) and for the surface renewal term according to eq. (6) are used. The equations reduce to

$$\begin{aligned} &\text{(K)} \quad \frac{\partial C_+}{\partial t_+} = \frac{\partial}{\partial z_+}\left[(1 + \alpha_{m+} z_+^m)\frac{\partial C_+}{\partial z_+}\right] \\ &\text{(SR)} \quad \frac{\partial C_+}{\partial t_+} = \frac{\partial^2 C_+}{\partial z_+^2} - \gamma_{p+} z_+^p\, C_+, \end{aligned} \tag{15}$$

where γ and α are given by

$$\begin{aligned} \alpha_{m+} &= \frac{\alpha_m z_*^m}{D} \\ \gamma_{p+} &= \gamma_p z_*^p. \end{aligned} \tag{16}$$

A.2. Steady state solutions

These equations are solved for the following boundary conditions

$$j_+ = \begin{cases} -\left.\dfrac{\partial C_+}{\partial z_+}\right|_{z_+ = 0} = 1 \\ \lim\limits_{z_+ \to \infty} \quad = 0. \end{cases} \tag{17}$$

The concentration profile for the K-model can be integrated directly

$$C_+ = 1 - \alpha_{m+}^{-1}\int_0^{z_+} \frac{1}{1 + (\alpha_m + z'_+)^m}\,\mathrm{d}z'_+ \tag{18}$$

where α_{m+} is given by

$$\alpha_{m+} = \int_0^\infty \frac{1}{1 + z'^m_+}\,\mathrm{d}z'_+ = \frac{\pi}{m\sin(\pi/m)}. \tag{19}$$

For $m = 2$, eq. (19) reduces to

$$\text{(K, } m = 2) \quad C_+ = \frac{2}{\pi}\operatorname{arccot}\left(\frac{\pi}{2} z_+\right). \tag{20}$$

It is noteworthy that the concentration integral over the boundary layer, S_+

$$S_+ = \int_0^\infty C_+\,\mathrm{d}z'_+ = \frac{m\sin^2(\pi/m)}{\pi\sin(2\pi m)} \tag{21}$$

reaches infinity in this case ($m = 2$).

For the SR-model only the classical case ($p = 0$) can be solved analytically. A simple exponential profile is obtained

$$\text{(SR, } p = 0) \quad C_+ = \mathrm{e}^{z_+}. \tag{22}$$

For $p = 1$, the concentration profile is given by the Airy function

$$\text{(SR, } p = 1) \quad C_+ = \frac{1}{\mathrm{Ai}(0)}\,\mathrm{Ai}\left(\frac{\mathrm{Ai}(0)}{\mathrm{Ai}'(0)} z_+\right). \tag{23}$$

(The prime denotes the z-derivative.) Ai(0) and Ai(0)/Ai(0)′ have the approximate values 0.3550 and 1.372, respectively.

For large p and m, and only for this condition,

both models coincide to the classical film model with a linear concentration profile

$$(\mathrm{D, SR}, p, m \to \infty) \quad C_+ = \begin{cases} 1 - z_+ & 0 \leqslant z_+ \leqslant 1, \\ 0 & z_+ > 1. \end{cases} \tag{24}$$

The different profiles are compared to each other in Fig. 16.

A.3. Dynamical solutions

Fourier transformation in time yields from (eq. 15) equations for the complex Fourier amplitudes $\tilde{c}_+(\omega_+)$

$$\begin{aligned} &(\mathrm{K}) \quad i\omega_+ \tilde{c}_+ = \frac{\partial}{\partial z_+}\left[(1 + \alpha_{m+} z_+^m)\frac{\partial \tilde{c}_+}{\partial z_+}\right] \\ &(\mathrm{SR}) \quad (i\omega_+ + \gamma_{p+} z_+^p)\tilde{c}_+ = \frac{\partial^2 \tilde{c}_+}{\partial z_+^2}, \end{aligned} \tag{25}$$

where $\omega_+ = \omega t_*$.

The boundary conditions are given, firstly, by the flux density applied at the surface. In Fourier space, this is the Fourier transform of any time changing flux density.

$$\left.\frac{\partial \tilde{c}_+}{\partial z_+}\right|_{z_+ = 0} = -\tilde{j}_+(\omega_+)$$
$$\lim_{z_+ \to \infty} \tilde{c}_+(z_+) = 0. \tag{26}$$

Again, these equations can be solved analytically only for a few cases (SR, $p = 0$, and p, $m \to \infty$ (film model F)

$$(\mathrm{SR}, p = 0) \quad \begin{aligned} \tilde{c}_+ &= \tilde{z}_e \exp(-z_+/\tilde{z}_e) \\ \tilde{j}_+ &= \exp(-z_+/\tilde{z}_e), \end{aligned} \tag{27}$$

where $\tilde{z}_e = (1 + i\omega_+)^{-1/2}$ is the (complex) effective penetration depth both for the concentration and the flux density.

Solution of the equations for the film model yields

$$(\mathrm{F}) \quad \begin{aligned} \tilde{c}_+ &= \frac{\sinh[\sqrt{i\omega_+}(1 - z_+)]}{\sqrt{i\omega_+}\cosh(\sqrt{i\omega_+})} \\ \tilde{j}_+ &= \frac{\cosh[\sqrt{i\omega_+}(1 - z_+)]}{\cosh(\sqrt{i\omega_+})}. \end{aligned} \tag{28}$$

The equations for the surface concentration ($z_+ = 0$) reduce to

$$\begin{aligned} &(\mathrm{SR}, p = 0) \quad \tilde{c}_+(0) = (1 + i\omega_+)^{-1/2} \\ &(\mathrm{F}) \quad \tilde{c}_+(0) = \frac{\tanh(\sqrt{i\omega_+})}{\sqrt{i\omega_+}}. \end{aligned} \tag{29}$$

From these equations, the amplitude damping of the surface concentration and the phase shift between the surface flux density and the surface concentration can be derived:

$$\begin{aligned} &(\mathrm{SR}, p = 0) \quad \begin{aligned} |\tilde{c}_+(0)| &= (1 + \omega_+^2)^{-1/4} \\ \varphi(0) &= \arctan \omega_+ \end{aligned} \\ &(\mathrm{F}) \quad \begin{aligned} |\tilde{c}_+(0)| &= \frac{1}{\sqrt{i\omega_+}} \frac{(\sin^2\sqrt{2\omega_+} + \sinh^2\sqrt{2\omega_+})^2}{\cos\sqrt{2\omega_+} + \cosh\sqrt{2\omega_+}} \\ \varphi(0) &= \arctan\left(\frac{\sinh\sqrt{2\omega_+} - \sin\sqrt{2\omega_+}}{\sinh\sqrt{2\omega_+} + \sin\sqrt{2\omega_+}}\right) \end{aligned} \end{aligned} \tag{30}$$

For all other models, general solutions can only be obtained by numerical models (see below).

A.4. Phase shift for small frequencies

For the important limiting case of small frequencies, a simple general solution for the phase shift of the surface concentration is possible. In this case, we can assume that only a phase shift and no amplitude attenuation occurs (Fig. 2). Therefore the complex concentration is given by

$$\tilde{c}_+ = C_+(z_+)\, e^{i\varphi(z_+)}. \tag{31}$$

With this formulation, the boundary condition at the surface, eq. (26) yields the simple relation

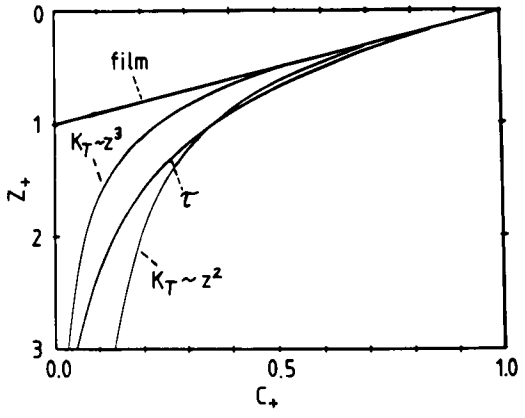

Fig. 16. Calculated mean boundary layer profiles for different models in a dimensionless plot: the film model, the SR-model $p = 0$, and the K-model for $m = 2$ and $m = 3$.

between the phase function and its z-derivative which is independent of any model assumptions

$$\varphi'(0) = \varphi(0). \tag{32}$$

Introducing this equation into eq. (25) yields

$$\begin{aligned} &\text{(SR)} \quad \varphi'' + \varphi' \frac{2C'_+}{C_+} = \omega_+ \\ &\text{(K)} \quad \varphi'' + \varphi' \left(\frac{2C'_+}{C_+} - \frac{C''_+}{C_+} \right) = \omega_+, \end{aligned} \tag{33}$$

with the following solutions for the phase shift at the surface

$$\begin{aligned} &\text{(SR)} \quad \varphi(0) = \omega_+ \int_0^\infty C_+^2 \, \mathrm{d}z_+ \\ &\text{(K)} \quad \varphi(0) = \omega_+ \int_0^\infty \frac{C_+^2}{C'_+} \, \mathrm{d}z_+. \end{aligned} \tag{34}$$

The latter formulas show a direct relation between the phase shift for low frequencies and the steady state concentration profile, and that this relation is different for the different models. From eq. (32), we conclude that the phase shift increases linearly at the surface with a slope equal to the phase shift at the surface

$$\varphi(z_+) = \kappa \omega_+ (1 + z_+), \tag{35}$$

where $\kappa = \varphi(0)/\omega_+$ can be calculated from eq. (34).

A.5. Numerical solutions

Numerical solutions of the steady state and dynamic concentration profiles were obtained by a simple box model. The following general iteration schema was applied to calculate steady state solutions of eq. (15):

$$\begin{aligned} C_+(j)^{(n+1)} = a_j^- \, C_+(j-1)^{(n)} + a_j C_+(j)^{(n)} \\ + a_j^+ \, C_+(j+1)^{(n)}, \end{aligned} \tag{36}$$

where j denotes the box number. The coefficients are calculated from the corresponding differential equations (eq. (15)) replacing the derivatives by finite differences. The coefficients for the SR-models, for example, are given by

$$\begin{aligned} a_j^- = a_j^+ = e = \frac{\Delta t_+}{(\Delta z_+)^2} \\ a_j = 1 - 2e - \Delta t_+ \gamma_p z_+^p, \end{aligned} \tag{37}$$

where Δt_+ and Δz_+ are the step widths in time and space, respectively. The variable e is the critical parameter for the iteration stability and was chosen to be $\leqslant 0.25$. Space intervals of $\Delta z_+ < 0.1$ lead to a sufficient accuracy of the calculations.

The strong increase of the turbulent diffusion coefficient K_t with z_+ constitutes a problem for the numerical solution of the K-models, since it forces the time step to be very low in order to achieve a stable iteration. The problem was avoided by a transformation of the z_+-coordinate, resulting in a box-size increasing with z_+. The following transformations were used

$$\begin{aligned} &\text{(K, } m = 2) \quad z_{+t} = \ln(1 + z_+) \\ &\text{(K, } m > 2) \quad z_{+t} = \frac{1}{(m-2)(1+z_+)^{m+2}}, \end{aligned} \tag{38}$$

resulting in complex formulas for the coefficients a_j, which are not shown here. It is worthwhile to note that for $m > 2$, the whole boundary layer profile is projected into the finite interval $[0, 1/(m-2)]$.

Profiles with the boundary condition of a sinusoidal surface flux are directly calculated with the complex concentration amplitudes $\tilde{c}_+$. From eq. (25), the following iteration scheme is derived

$$\begin{aligned} \tilde{c}_+(j)^{(n+1)} = a_j^- \, \tilde{c}_+(j-1)^{(n)} + (a_j + i\omega_+ \Delta t_+) \tilde{c}_+(j)^{(n)} \\ + a_j^+ \, \tilde{c}_+(j+1)^{(n)}, \end{aligned} \tag{39}$$

with the same real coefficients as in eq. (36).

The boundary condition of a constant flux density at the surface is accommodated by assuming a virtual box above the interface (with the index 0) whose concentration can be calculated by

$$\tilde{j}_+ = \left. \frac{\partial \tilde{c}_+}{\partial z_+} \right|_{z_+ = 0} \approx \frac{\tilde{c}_+(2) - \tilde{c}_+(0)}{2\Delta z_+}, \tag{40}$$

resulting in

$$\tilde{c}_+(0) = \tilde{c}_+(2) + 2\Delta z_+, \tag{41}$$

thus maintaining a constant flux at the interface. The results of the numerical calculations are discussed in the text.

A.6. Corrections for non-zero penetration of the source term

All calculations up to this point have been carried out using a constant flux at the interface.

But since the IR-radiation used in the experiments penetrates a certain depth into the surface layer, a distributed source term $Q_+(z_+)$ with a certain penetration depth z_r is a more realistic assumption. The flux density j_+ is given as the integral over the source term

$$j_+(z_+) = \int_0^{z_+} Q_+(z'_+)\,dz'_+. \tag{42}$$

Since it is known (compare Fig. 4) that the radiative penetration depth z_r is small compared with the boundary layer thickness ($z_r \ll z_*$), the deviations from the solution for a non-penetrating source can be calculated without any assumptions about the turbulent structure in the boundary layer. This follows since the radiative penetration is limited to the region exclusively dominated by molecular diffusion. In this region, the differential equation for the complex concentration amplitude reads

$$\frac{\partial^2 \tilde{c}_+}{\partial z_+^2} - i\omega_+ \tilde{c}_+ = Q_+(z_+). \tag{43}$$

The boundary condition at the surface is now given by

$$\left.\frac{\partial \tilde{c}_+}{\partial z_+}\right|_{z_+=0} = 0, \tag{44}$$

since no source is at the interface itself. In addition, for $z_+ \gg z_{r+} = z_r/z_*$, the solution is equal to the solution for a flux just at the surface, as long as the diffusive penetration depth z_{d+} is larger than z_{r+}, since then the underlying part of the boundary layer is driven by the same flux density. For steady state conditions ($\omega_+ = 0$), eq. (43) is integrable and yields

$$C_+(z_+) = C_+(0) - \int_0^{z_+} j_+(z'_+)\,dz'_+. \tag{45}$$

If the depth z_+ is large enough, say $z_{+0} \gg z_{r+}$, all IR-radiation is absorbed and the integrand is constant. Then, the shape of the profile coincides with the linear concentration profile close to the surface ($z_{+0} \ll 1$) given by

$$C_+(z_{+0}) = 1 - z_{+0}. \tag{46}$$

From both equations we yield the surface concentration $C_+(0)$

$$C_+(0) = 1 - z_{+0} + \int_0^{z_+0} j_+(z_+)\,dz_+. \tag{47}$$

This is a very simple equation if we use the second two terms to define the radiative penetration depth z_+ as

$$z_{r+} = \int (1 - j_+(z_+))\,dz_+. \tag{48}$$

(For an exponential source term $Q(z) = 1/z_{e+} \exp(-z_+/z_{e+})$ we indeed get $z_{r+} = z_{e+}$.) Eq. (47) then reduces to

$$C_+(0) = 1 - z_{r+}. \tag{49}$$

So far we have only discussed the steady-state solution, but it is possible to derive a general formula even for the case of small chopper frequencies $\omega_+ < 1$. The basic argument comes from the fact that the solution simply contains a small additive imaginary term, which is a solution of the corresponding homogeneous equation to eq. (43), since the source term is real. This fact leads to the following simple solution for the surface concentration

$$C_+(0) = 1 - z_{r+} - i\kappa\omega_+. \tag{50}$$

Consequently, the decrease in the surface amplitude is still proportional to z_{r+}. Now we also know that the phase shift is slightly increased by the same factor

$$\varphi = \kappa\omega_+(1 + z_{r+}). \tag{51}$$

Eq. (50) allows another simple interpretation. If, under the condition of a constant flux density, the measured surface concentration is decreased by a certain factor, the transfer velocity is increased by the same factor according to eq. (1), and the measured boundary layer thickness, z_{*m}, is decreased equally (eq. (4))

$$z_{*m}/z_* = 1 - z_{r+} = 1 - z_r/z_*. \tag{52}$$

Thus, we finally arrive at the simple conclusion that the real boundary layer thickness is just given by the measured value plus the radiation penetration depth z_r

$$z_* = z_{*m} + z_r. \tag{53}$$

REFERENCES

Broecker, H.-C., Petermann, J. and Siems, W. 1978. The influence of wind on CO_2-exchange in a wind-wave tunnel, including the effects of monolayers. *J. Marine Res. 36*, 595–610.

Broecker, W., Ledwell, J. R., Takahashi, T., Weiss, R., Merlivat, L., Memery, L., Peng, T.-H., Jähne, B. and Münnich, K. O. 1986. Isotopic versus micrometeorologic ocean CO_2 fluxes: a serious conflict. *J. Geophys. Res. 91*, 10,517–10,527.

Brutsaert, W. and Jirka, G. H., eds. 1984. *Gas transfer at water surfaces*. Dordrecht/Holland: Reidel.

Coantic, M. 1986. A model of gas transfer across air–water interfaces with capillary waves. *J. Geophys. Res. 91*, 3925–3943.

Hasse, L. 1971. The sea surface temperature deviation and the heat flow at the sea–air interface. *Boundary Layer Meteor. 1*, 368–379.

Jähne, B. 1982. Dry deposition of gases over water (gas exchange). In *Exchange of pollutants at the air/earth interface (dry deposition)* (ed. D. Flothmann). Battelle Institut Frankfurt am Main, BleV-R-64.284-2 (in German).

Jähne, B. 1985. *Transfer processes across the free water surface*. Habilitationsschrift, Faculty for Physics und Astronomy, Heidelberg University, F.R.G.

Jähne, B., Münnich, K. O. and Siegenthaler, U. 1979. Measurements of gas exchange and momentum transfer in a circular wind-water tunnel. *Tellus 31*, 321–329.

Jähne, B., Huber, W., Dutzi, A., Wais, T. and Ilmberger, J. 1984. Wind/wave-tunnel experiments on the Schmidt number and wave field dependence of air–water gas exchange. In *Gas transfer at water surfaces* (eds. W. Brutsaert and G. H. Jirka). Dordrecht/Holland: Reidel, 303–309.

Jähne, B., Münnich, K. O., Bösinger, R., Dutzi, A., Huber, W. and Libner, P. 1987a. On the parameters influencing air–water gas exchange. *J. Geophys. Res. 92*, 1937–1949.

Jähne, B., Heinz, G. and Dietrich, W. 1987b. Measurements of the diffusion coefficients of sparingly soluble gases in water. *J. Geophys. Res. 92*, 10,767–10,776.

Kitaigorodskii, S. A. 1984. On the fluid dynamical theory of turbulent gas transfer across an air–sea interface in the presence of breaking wind-waves. *J. Phys. Oceangr. 14*, 960–972.

Libner, P. 1987. The controlled flux method: a new fast and local method for investigating exchange processes at the air–water interface. Dissertation, Faculty for Physics und Astronomy, Heidelberg University, F.R.G. (in German).

Libner, P., Jähne, B. and Plate, E. 1987. A new method measuring water reaeration locally and fast (in German). *Wasserwirtschaft 77*, 230–235.

Liss, P. S. and Slater, P. G. 1974. Flux of gases across the air/sea interface. *Nature 247*, 181–184.

McCready, M. J. and Hanratty, T. J. 1984. A comparison of turbulent mass transfer at gas–liquid and solid–liquid interfaces. In *Gas transfer at water surfaces* (eds. W. Brutsaert and G. H. Jirka). Dordrecht/Holland: Reidel, 283–292.

Paulson, C. A. and Simpson, J. J. 1981. The temperature difference across the cool skin of the ocean. *J. Geophys. Res. 86*, 11044–11054.

Plate, E. and Friedrich, R. 1984. Reaeration of open channel flow. In *Gas transfer at water surfaces* (eds. W. Brutsaert and G. H. Jirka). Dordrecht/Holland: Reidel, 333–346.

Roether, W. 1983. Field measurement of air-sea gas transfer: a methodical search. *Boundary Layer Meteor. 27*, 97–103.

Roether, W. and Kromer, B. 1984. Optimum application of the radon deficit method to obtian air–sea gas exchange rates. In *Gas transfer at water surfaces* (eds. W. Brutsaert and G. H. Jirka). Dordrecht/Holland: Reidel, 447–457.

Wanninkhof, R., Ledwell, J. R. and Broecker, W. S. 1985. Gas exchange–wind speed relation measured with sulfur hexafluoride on a lake. *Science 227*, 1224–1226.

Wanninkhof, R., Ledwell, J. R., Broecker, W. S. and Hamilton, M. 1987. Gas exchange on Mono Lake and Crowley Lake California. *J. Geophys. Res. 92*, 14,567–14,580.